Heliyon

Development of a hybrid CFD-PBPK model to predict the transport of xenon gas around a human respiratory system to systemic regions

Ahmadreza Haghnegahdar, Jianan Zhao, Max Kozak, Patrick Williamson, Yu Feng[*]

School of Chemical Engineering, Oklahoma State University, Stillwater, OK 74078, USA

[*] Corresponding author.

E-mail address: yu.feng@okstate.edu (Y. Feng).

Abstract

Administering incorrect doses of conventional anesthetic agents through the pulmonary route can cause potential health risks such as blood coagulation, platelet dysfunction, and deteriorating organ function. As an alternative, xenon can minimize the impact on the cardiovascular system and provide the neuroprotective effect, hemodynamic stability, and fast recovery. However, the inhalation pattern still needs to be carefully monitored and controlled to avoid health risks caused by over administering xenon to patients during unconsciousness. Thus, high-resolution lung absorption and whole-body translocation data are critically needed to fully understand how to administer the gas and coordinate with the patient to accurately control the dose. Clinical studies are not able to provide accurate dosimetry data due to their limited operational flexibility and imaging resolution. Therefore, a computational fluid dynamics (CFD) model was employed in this study to simulate the transport and absorption of the inhaled xenon which is connected with a physiologically based pharmacokinetic (PBPK) model to predict the translocation into the systemic regions. To study the effects of different breathing patterns on xenon transport dynamics in the human body, a realistic breathing waveform and two steady-

state flow rates with inhalation durations of 2 and 1.5 seconds were selected. For the realistic breathing cycle, the inhalation-exhalation periods are defined for a human at rest and the other two cases have a fixed volumetric flow rate of 15 L/min. As the two latter cases only simulate the inspiratory phase, a 1-second holding time was applied to represent the missing periods of the full breathing time. Simulations were performed in a subject-specific human upper airway configuration from mouth to G6. Numerical results show that with the accurate lung uptake predictions obtained from the CFD model, the hybrid CFD-PBPK model with TRANSIT compartments generates more precise and breath-specific trends compared to simple PBPK models. Numerical results demonstrate that breathing pattern can significantly influence the xenon uptake in the human body, which can be utilized as a critical factor to be coordinated by clinicians to achieve the optimized xenon dose. Furthermore, parametric analyses were performed for the influence of breathing patterns on local airflow distributions, gas species translocations, and lung elimination mechanisms followed by species diffusion into the systemic regions.

Keywords: Mechanical engineering, Pharmaceutical science

1. Introduction

Xenon is of particular interest for use as an anesthetic agent, because it is a quite unreactive substance in the body and is exceptionally insoluble in human tissue (Goto et al., 1997). Therefore, xenon is highly removable from the lungs without interfering with the surrounding renal and hepatic systems, or other tissues (Bedi et al., 2003; Reinelt et al., 2002). The most realistic method of administering xenon in a clinical setting is through a continuous, closed-loop recycle stream. Xenon consumption in a closed-loop stream generally has a wash-in phase where the injection is set to 2 L/min. After the wash-in phase, the closed-loop recycle stream is generally set such that xenon is injected at a rate that allows for maintenance of the oxygen concentration in the body (Stoppe et al., 2013). Since a reliable closed-loop system has already been developed, xenon could conceivably become an applicable anesthetic, especially for patients who need extra cardiovascular and neuroprotective advantages. At the same time, research has shown that xenon has a blood-gas partition coefficient that is significantly lower than other clinically used anesthetics, making the use of xenon more effective on the patient's body (Goto et al., 1998; Sanders et al., 2003). Subsequently, the use of xenon as an anesthetic gas (AG) also results in both a rapid induction and later a rapid emergence from unconsciousness, which is a desirable effect of an anesthetic for humans. Researchers have also completed works considering xenon's biological effects such as activation of pro-survival signaling pathways and potassium channel activation (Katz et al., 2015).

Although xenon has already been approved for use as an AG, it is important to conduct further studies to determine the range of xenon concentration that can be administered for safe and efficient use on patients. To date, multiple studies show that xenon can be optimally used as an anesthetic agent when it is in a mixture with 30% oxygen (Lynch et al., 2000). However, studies also claim if the volume fraction is higher than 60%, a significant amount of xenon retention was found in the fatty tissues and bowels (Luttropp et al., 1993), while the cerebral blood flow also increases accordingly (Lynch et al., 2000). The finding mentioned above triggers the interests to further investigate the safe range of xenon administration in various clinical surgeries.

A study by Sanders et al. (2005) demonstrated that xenon at a concentration of 60 ± 5% was not only safe for the patients but was even proven to have a faster recovery time than using isoflurane and nitrous oxide, which are two widely used anesthetic agents. An estimation by Goto et al. (2002) shows that in a middle-aged group of patients, the minimum alveolar concentration (MAC) of xenon (calculated as xenon concentration in an atmosphere that would reduce the MAC of sevoflurane to 0%) is approximately 63%, which is similar to the estimation of the aforementioned results (Sanders et al., 2005). Also, Goto et al. (2002) discovered significant gender dependency among senior patients (≥65 years). Specifically, older females have a significantly lower MAC than males. The MAC value induced by xenon inhalation is 51% for senior women and 69% for men (Goto et al., 2002). Such a difference among different senior patients also indicates both the efficacy and the sensitivity of applying xenon on certain patients for anesthesia purpose. Those lowered effective ranges of xenon concentration reduce the concern regarding xenon gas retention in the surrounding tissues and cerebral blood flow. Additionally, Eger (2001) demonstrated that for anesthetics in general, MAC decreases with the increase in patient age. Thus, existing studies proved the necessity of using personalized inputs to reflect inter-subject variabilities when performing the anesthetic effectiveness assessment of xenon administration to guarantee the predicting accuracy.

In addition to the discussion on the effects of administering xenon gas throughout the respiratory system and surrounding tissues over specific concentration ranges, it is believed that xenon has the potential to be an especially effective anesthetic for reducing a secondary injury of the brain after an initial trauma and could provide reliable neuroprotective advantages (Coburn et al., 2008). A study by Coburn et al. (2008) indicated that xenon could be particularly beneficial for use on patients with traumatic brain injury. It also indicates that the use of xenon as an anesthetic agent would not have any significant adverse impacts on the brain.

Studying the pharmacokinetics (PK) of xenon is essential for scientists and anesthesiologists to minimize the administration dose and guarantee the anesthesia's effectiveness. Therefore, numerical models can be beneficial, since they can accurately predict xenon transport inside the human body in a noninvasive and cost-effective manner. However, clinical studies are scarce, and model optimizations or validations using patient-specific clinical data are challenging. Extrapolation from animal studies to humans is usually necessary in order to speculate the human effects of different administrations. One of the first *in vivo* studies using animals (Nalos et al., 2001) measured xenon concentration time courses during the wash-in phase of pigs. They observed that the equilibrium concentration occurred at 7 minutes. Lockwood (2010) studied the elimination time of xenon from the brain, and using interspecies extrapolations he claimed that xenon was eliminated faster in the brain compared to other AGs such as halothane, enflurane, isoflurane, sevoflurane, and desflurane. Later, Katz et al. (2015) also applied a physiologically based pharmacokinetic (PBPK) model and investigated the continuous administration of xenon with repeated dosing. Model validations were performed by comparing their PBPK results with experimental studies (Lockwood, 2010; Nalos et al., 2001). However, several limitations exist in these studies, including the capability to employ human breathing pattern effect, which can significantly influence the translocation of the anesthetic agent in the systemic regions.

Unadjusted induction of the inspired xenon can be harmful to patients. Additionally, no *in silico* investigation has been reported on the residual concentration of xenon throughout the human respiratory system and systemic regions after realistic longterm inhalations. By coupling a PBPK model with a computational fluid dynamics (CFD) model, the objective of this study is to perform multiscale simulations to predict local absorption and transport of xenon from a subject-specific human respiratory system to systemic regions in the whole body with different inhalation patterns. Specifically, by developing the experimentally validated CFD-PBPK model, this study provides a new tool to evaluate the effectiveness and health risks of pulmonary anesthetic administration. Not only does this study provide insight into the practicality of using xenon as an inhalable anesthetic agent for patient use, but it also provides the opportunity to evaluate the feasibility of using the coupled CFD-PBPK model to investigate the transport and absorption of other inhaled AG in the respiratory system. The CFD-PBPK model demonstrates the effect of a patient-specific breathing pattern on the uptake concentration and absorption within the respiratory system.

2. Methodology

Governed by first principles, the CFD-PBPK model is a promising tool to assess the continuous exposure health risks of pharmaceutical chemicals. Integrating

complete multiscale model validation and optimization, the hybrid CFD-PBPK model provides specific information about how different levels of administration may affect the bioavailability of a substance in the human systemic regions, thereby potentially influencing a patient's health. The CFD and PBPK models for inhaled AG are developed and validated (see Sections 2.4.5 and 2.4.6). The flowchart of the two-way coupling algorithm is presented in Fig. 1. The CFD model is initialized with the approximate mass fraction of oxygen in the air, i.e., 23.3%. Also, two consecutive breathing cycles are simulated. The first cycle is initialized with zero concentration of xenon. However, the 2nd cycle is started with the calculated xenon concentration from the last time-step of the previous breathing cycle. The concentrations at airway walls are calculated to define the initial conditions of the post-absorption calculation for the transport of xenon into the systemic regions. Simultaneously, the change in the arterial pool at the end of transient CFD calculation is evaluated using a PBPK model, by estimating the balance of the chemical potential at the airway walls for the following time step. In this study, 3 breathing scenarios are considered with the following breathing patterns:

- Case 1: Realistic breathing pattern (Scheinherr et al., 2015) including 1.76-s inhalation period and 4.02-s total period of a breathing cycle (average total tidal volume of 686 mL),

- Case 2: 2.0-s inhalation, 1.0-s holding, at a constant flow rate of 15 L/min, and

- Case 3: 1.5-s inhalation, 1.0-s holding, at a constant flow rate of 15 L/min.

Case 1 considers a realistic human respiratory waveform at rest, while Cases 2 & 3 can represent the inhalation phases of different mechanical ventilation scenarios (Barrett, 2010). The governing equations are listed as follows.
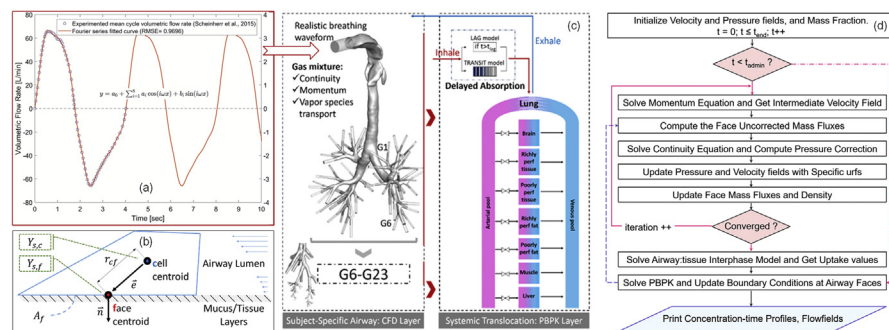

Fig. 1. Modeling framework of the hybrid CFD-PBPK model: (a) Realistic breathing waveform (Case 1); (b) Sketch for the 3rd-type boundary condition at airway walls; (c) The coupling mechanisms between CFD and PBPK models; and (d) The flowchart of iterations.

2.1. Computational fluid dynamics (CFD) model

2.1.1. Governing equations for anesthetic gas (AG) mixture

Inhaled xenon and oxygen form a gas mixture at standard ambient conditions and can be modeled as a continuous mixture phase. The governing equations can be given as:

2.1.1.1. Continuity equation

$$\frac{\partial \rho}{\partial t} + \frac{\partial (\rho u_i)}{\partial x_i} = 0 \tag{1}$$

in which u_i represents vethe locity vector of the mixture.

2.1.1.2. Momentum equation

$$\rho \left(\frac{\partial u_i}{\partial t} + u_j \frac{\partial u_i}{\partial x_j} \right) = -\frac{\partial p}{\partial x_i} + \frac{\partial}{\partial x_j} \left[(\mu + \mu_t) \left(\frac{\partial u_i}{\partial x_j} + \frac{\partial u_j}{\partial x_i} \right) \right] + \rho g_i \tag{2}$$

where μ is the gas mixture molecular dynamic viscosity, ρ is the density of the mixture, and μ_t is the turbulent viscosity. Constants are obtained from Wilcox (1998).

At typical human respiratory flow rates, from 15 to 60 L/min, laminar-to-turbulence transitional flow occurs in upper airways. Zhang and Kleinstreuer (2011) analyzed and compared low Reynolds number (LRN) $k - \omega$ model, standard $k - \omega$ model, and shear stress transport (SST) transition model (Menter et al., 2006a, 2006b). They discovered that the SST transition model could accurately predict the transitional turbulence regime by selecting appropriate constants. Therefore, the SST transition model is adopted in this study.

2.1.1.3. Convection-diffusion equations for anesthetic gas (AG) species

AG contains multiple species, specifically xenon (Xe) and oxygen (O_2). The convection-diffusion equation is introduced to describe the transport of the Xe and O_2 mass fractions in human lung airways, i.e.,

$$\rho \frac{\partial Y_s}{\partial t} + \rho \frac{\partial (u_i Y_s)}{\partial x_i} = \frac{\partial}{\partial x_i} \left[\left(\rho D_{a,s} + \frac{\mu_t}{Sc_t} \right) \frac{\partial Y_s}{\partial x_i} \right] \tag{3}$$

where Y_s is the mass fraction of species s, $D_{a,s}$ is the binary diffusivity of species s in the gas mixture, $Sc_t = 0.9$ is the turbulence Schmidt number, and μ_t is the turbulence viscosity (Zhang et al., 2012a, 2012b).

2.1.1.4. Gas absorption at airway walls

The third-type boundary conditions are employed at the human-airway surface to calculate the xenon absorption rate. It has been used in the previous study (Feng et al., 2016) and was shown to have more accurate and closer to realistic condition than the first-type boundary conditions (Keyhani et al., 1997). Specifically, the third-type boundary conditions can be given as:

$$\Psi_s^{-1}\frac{\partial Y_{s,c}}{\partial x_i}\boldsymbol{n_i}A_f = \left(Y_{s,f} - Y_{s,\infty}\right)A_f \tag{4}$$

where $Y_{s,f}$ represents the mass fraction of the xenon and oxygen in the mucous membrane lining, A_f is the control volume face surface, and $\boldsymbol{n_i}$ is the outward unit normal vector of A_f (see Fig. 1). Katz et al. (2015) and Lockwood (2010) advocated the perfusion limited model for the transport of xenon in the tissue site, because of the fast diffusion characteristics. Accordingly, the absorption coefficient for the two-resistance model is defined as (Treybal, 1980):

$$\Psi_s = \frac{D_{w,s}}{D_{a,s}H_{c,s}z_m} \tag{5}$$

where $D_{w,s}$ and $H_{c,s}$ denote the diffusivity of the gas species in mucus layers and the Henry's law constant respectively. Eq. (4) represents the air-mucus interphase mass balance based on the equality of the species chemical potential and is defined based on two assumptions, i.e., (1) the rate of transport is instantaneous and equilibrium prevails at all times at the interface, (2) the rate of transport is controlled by the rates of diffusion through the phases. To define Henry's law constants, the air-water equilibrium was employed to represent air-mucus equilibrium (Feng et al., 2016). Constant mucus layer thickness $z_m = 10 \, \mu m$ is assumed at all inner walls of the human upper airway (ICRP, 1994).

Eq. (4) was numerically solved using the midpoint rule. Specifically, $\frac{\partial Y_{s,c}}{\partial x_i}$ was approximated using the implicit term (at the current iteration) and explicit term (obtained from the previous iteration), i.e.,

$$\frac{\partial Y_{s,c}}{\partial x_i}\boldsymbol{n_i}A_f \approx \frac{\left(Y_{s,f} - Y_{s,c}\right)}{r_{cf}}\frac{A_f}{\boldsymbol{e_i}\boldsymbol{n_i}} + \left(\left.\frac{\partial Y_{s,c}}{\partial x_i}\right|_{iter-1}\boldsymbol{n_i}A_f - \left.\frac{\partial Y_{s,c}}{\partial x_i}\right|_{iter-1}\boldsymbol{e_i}\left(\frac{A_f}{\boldsymbol{e_j}\boldsymbol{n_j}}\right)\right) \tag{6}$$

where A_f and $\boldsymbol{n_i}$ are the surface area and the normal vector of the mesh element face. $\frac{\partial Y_{s,c}}{\partial x_i}\boldsymbol{n_i}A_f \approx \frac{\left(Y_{s,f}-Y_{s,c}\right)}{r_{cf}}\frac{A_f}{\boldsymbol{e_i}\boldsymbol{n_i}} + \left(\left.\frac{\partial Y_{s,c}}{\partial x_i}\right|_{iter-1}\boldsymbol{n_i}A_f - \left.\frac{\partial Y_{s,c}}{\partial x_i}\right|_{iter-1}\boldsymbol{e_i}\left(\frac{A_f}{\boldsymbol{e_j}\boldsymbol{n_j}}\right)\right)$ and e_i are the cell-to-face centroid distance and unit normal vector respectively. Using Eqs. (4)

Table 1. Physiochemical parameters of the compartmental tissues for the prediction of Xe translocation.

Compartment Name	Volume [L]	Blood Flow [L/min]	Tissue/Blood PC
Arterial Pool	1.46	6.00	1.00
Venous Pool	3.82	6.00	1.00
Lung Blood	0.17	6.00	0.14
Fat (Richly Perfused)	6.30	0.24	9.29
Fat (Poorly Perfused)	4.20	0.06	9.29
Liver	4.37	1.56	0.54
Tissue (Richly Perfused)	16.80	1.98	0.54
Tissue (Poorly Perfused)	30.80	0.06	0.54
Muscle	1.23	1.44	0.54
Brain	1.46	0.56	0.56
Body Weight [kg]		70.00	
Cardiac Output [L/min]		6.00	

and (6), $Y_{s,f}$ can be expressed by $Y_{s,c}$ and the mixed boundary condition can be achieved.

In this study, $Y_{s,\infty} = 0$ is assumed as the species mass fraction at the tissue compartment, which indicates the rapid removals of both oxygen and xenon via blood circulation. In addition, the species mass flux at the near wall elements (from airflow to mucus layer) can be defined by:

$$j_s = \rho D_{a,s} \frac{\partial Y_{s,c}}{\partial x_i} \boldsymbol{n_i} = \frac{\rho D_{w,s}}{H_{c,s} z_m} Y_{s,f} \qquad (7a,b)$$

where species-mucus diffusivities $D_{w,s}$ are given in Table 1.

2.2. Physiologically based pharmacokinetic (PBPK) model

The prediction of the transport from the airways to the systemic region is performed by calculating the absorption in the upper airways (CFD model) and the translocation in the lower airways (compartmental PBPK). Therefore, a perfusion-limited PBPK model for multiple coupled organs was developed in the systemic regions. The model is governed by the generalized time-dependent ordinary differential equation (ODE) shown as follows:

$$V_T \frac{d}{dt} C_T = Q_T \cdot \left(C_{T,\,in} - \frac{C_T}{K_T} \right) \qquad (8)$$

where V, Q, C, and K are the organ's (or tissue with the subscript T) volume, flow rate, xenon concentration, and tissue-blood partition coefficient, respectively. Also,

$C_{T, in}$ is the input concentration to the organs which is defined by the concentration at the arterial pool. Xenon is a quite unreactive substance in the body (Goto et al., 1997) and is essentially transported in the body without interfering with the surrounding renal and hepatic systems, as demonstrated in previous studies by Bedi et al. (2003) and Reinelt et al. (2002). In this regard, the reaction of xenon after absorption by the tissue is neglected in the development of this model. Moreover, the input concentration for the venous pool is the averaged amalgamation of interconnected organs to the venous pool, which is given by:

$$C_{T, in} = \frac{1}{Q_V} \sum_T Q_T (C_T / K_T) \tag{9}$$

where Q_V is equal to the cardiac output, representing the total volumetric flow rate of blood circulation. All the parameters including the volume and flow rate of organs, cardiac output, alveolar ventilation, body weight, and blood-gas partition coefficient were obtained from the open literature (Katz et al., 2015). However, the partition coefficients for liver, tissue-rich, tissue-poor, muscle, and brain compartments were revised. Table 1 presents the physiochemical properties of the xenon transport. It is worth mentioning that the PBPK model is able to predict the effect of absorption delay by integrating the TRANSIT and LAG models (Savic et al., 2007). In detail, the LAG model is shifting the time of absorption as if the chemical was administered later by adding a delayed absorption time to the uptake value. The TRANSIT model is a series of compartments (n) with an optimized transfer coefficient (k_{tr}). Having these compartments will dampen the effect of tidal chemical discharge into the systemic regions from the lungs. In this study, only two compartments are considered as the airway lumen is surrounded by epithelial and subepithelial layers.

2.3. Interconnection between the CFD and PBPK models

Mucus, epithelial, and subepithelial layers form the barrier between lung airways and blood circulation. To achieve the interconnection between CFD and PBPK models, the area-weighted averaged regional mass fraction $Y_{S,R}$ at airway walls was first calculated by:

$$Y_{s,R} = \frac{\sum_{wall} Y_{s,f} A_f}{\sum_{wall} A_f} \tag{10}$$

Subsequently, the uptake concentration ($C_{VU,s}$) can be calculated by:

$$C_{VU,s} = \sum_R \frac{Y_{s,R} \, \rho \, (BV)}{A_R \, z_m} \tag{11}$$

where $A_R = \sum_{wall} A_f$ is the regional surface area and BV denotes the breathing volume which can be defined as follows:

$$BV = \int\limits_{0}^{t} Q(t)\, dt \qquad (12)$$

In this equation, $Q(t)$ is the transient volumetric flow rate (see Section 2.4.3). The TRANSIT model is employed as:

$$C_{s,R,i} = k_{tr} C_{s,R,(i-1)} - k_{tr} C_{s,R,i} \qquad (13)$$

where $C_{s,R,i}$ is the regional uptake concentration at the tissue compartment i, Specifically, i = 1 means the epithelium and i = 2 means the subepithelium. The inlet to the first compartment (i = 1) is equal to the uptake concentration $C_{s,R,0} = C_{VU,s}$.

Assuming that the partition equilibrium will always be satisfied, the material mass balance equation for xenon can be given by (Katz et al., 2015; Lockwood, 2010):

$$C_A = 0.9 \frac{(0.9\, AV\, C_{G6-23}) + (CO\, C_V) + (C_{s,R,n} - C_L)\sum_R A_R\, z_m}{CO + \frac{0.9\, AV}{PC}} + 0.1 C_V \qquad (14)$$

In Eq. (14), AV is the alveolar ventilation (4.875 L/min), CO is cardiac output (6 L/min), and PC = 0.14 is the gas-blood partition coefficient for a human. Also, C_A, C_V, and C_L are the concentrations in arterial, venous, and lung compartments, respectively. In addition, C_L is the concentration at blood flow from the right ventricle. In addition, C_{G6-23} represents the transient xenon concentration escaping from the CFD domain and entering distal airways from G6 to G23. $C_{s,R,n}$ is the xenon concentration entering the systemic regions from mouth to G6, which can be calculated by Eq. (13). The accumulation of $C_{s,R,n}$ and C_{G7-23} indicates the concentration at the blood flow to the left atrium.

2.4. Numerical setup

2.4.1. Geometry

The subject-specific geometry from mouth to G6 airway model was reconstructed from the Magnetic Resonance Imaging (MRI) data (Zhang et al., 2012a). There is a 36 mm long extending cylindrical wall connecting the mouth and the inlet, and the diameter of the inlet is 20 mm. The total area of all lobe outlets is 846.976 mm². Fig. 2 shows the geometry and finite volume mesh details. The lobe segmentation is based on our in-house decomposition.

2.4.2. Mesh generation and independence test

Unstructured hybrid CFD meshes were generated using Fluent Meshing v. 19.1 (ANSYS Inc., Canonsburg, PA). Six near-wall prism layers were generated with the refined thickness to guarantee $y^+ < 1$ and to capture the laminar-to-turbulence transition sites correctly, where y^+ is the dimensionless wall distance (Lesieur and Moreau,
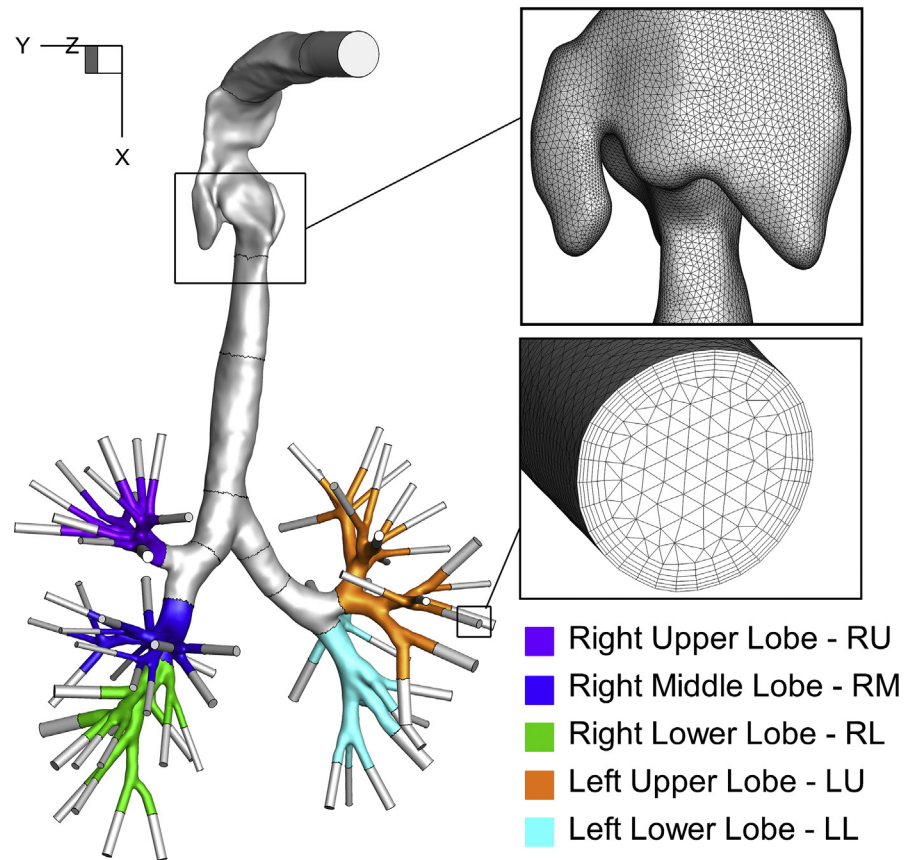
Fig. 2. The subject-specific human respiratory system and the final mesh details.

2008). The final mesh contains 13,493,089 elements and 4,069,940 nodes. Mesh independence tests were performed using steady-state airflow simulation with an inhalation flow rate $Q_{in} = 30$ L/min using the SST transition model. The wall boundary conditions were set to be no-slip and outlets were set to be uniform pressure outlets during inhalation. During the exhalation, an exponential decrease was assumed for the flow that will be discharged to the upper airways. Mesh topologies were determined by refining the meshes until grid independence of the flow field solutions was achieved.

2.4.3. Initial and boundary conditions

Table 2 presents the boundary condition and the required properties of oxygen and xenon. As inlet conditions, different velocity profiles were assigned to the three cases simulated in this study. For Case 1, a realistic breathing pattern was employed by an 8-term Fourier series fitting the experimental volumetric flow rate data (Scheinherr et al., 2015) representing a normal human breath at rest (see Fig. 1). The converted average velocity was applied as a uniform velocity profile at the mouth inlet with 20 mm in diameter. Also, the wall boundary conditions at the extended regions of the mouth inlet and truncated airway terminals are defined as zero absorption rate, since

Table 2. Boundary conditions and properties for the CFD-PBPK model setup.

Pressure [atm]			1.0
Temperature [K]			310.150
Inlet Velocity [L/min]	See Fig. 1 (Case 1), 15 (Cases 2 & 3)		
Mouth Inlet Diameter [mm]			20

Respired Components	Xenon	Oxygen	Mixture
Density[a] [kg/m^3]	5.710	1.429	5.133
Viscosity[b] [kg/m/s]	2.32e-05	2.06e-05	2.38e-05
Molecular Weight	131.293	15.990	
Volume fraction	0.670	0.330	
Mass fraction	0.888	0.111	
Diffusivity in water [m^2/s]	3.79e-09[c]	3.46e-09[d]	
Diffusivity in gas phase[e] [m^2/s]	1.37e-5	1.37e-5	
Dimensionless Henry's constant[f]	7.48e-7	6.19e-7	
Absorption coefficient [1/m]	3.67e+7	4.05e+7	

Data Sources:
[a] http://compost.css.cornell.edu.
[b] https://www.engineeringtoolbox.com.
[c] Weingärtner et al. (1992).
[d] http://compost.css.cornell.edu/oxygen/oxygen.diff.water.html.
[e] Calculated by Hirschfelder-Bird-Spotz method. Binary system diffusivity $D_{AB} = D_{BA}$.
[f] http://webbook.nist.gov.

these regions are not the realistic parts of the human respiratory geometry (see Fig. 2). For initial conditions, zero velocity fields are applied for all three cases, and the initial gas composition is assumed to be 23.3% O_2 and 0.0% Xe.

2.4.4. Discretization schemes

The numerical solution of the governing equations with appropriate boundary conditions was performed by using a user-enhanced, commercial finite-volume based program, i.e., ANSYS Fluent 19.1 (ANSYS Inc., Canonsburg, PA). All variables, including velocity components, pressure, turbulence variables, xenon gas transport, and absorption data were calculated and located at the centroids of the discretized mesh cells. Numerical simulations were performed on a local 64-bit Dell Precision T7910 workstation with 256 GB RAM and 16 3.1GHz processors and the supercomputers in the High-Performance Computing Center at Oklahoma State University (e.g., Cowboy cluster machine with 252 standards compute nodes with dual Intel Xeon E5-2620 "Sandy Bridge" hex core 2.0 GHz CPUs, with 32 GB of 1333 MHz RAM). The 2nd-order upwind scheme was used for the momentum equation calculation as well as the species transport equation. The system of ODEs of the PBPK model was solved using the 4th order Runge−Kutta method. The PBPK solver was written in C and compiled as user-defined functions (UDFs) in ANSYS Fluent.

Time steps are 0.02 s and 0.01 s for the CFD and PBPK parts respectively. The flow-chart in Fig. 1 shows how governing equations were coupled and solved iteratively.

2.4.5. CFD model validation

The CFD model employed in this study has been well validated in existing publications (Feng et al., 2017; Zhang et al., 2012a, 2012b). Specifically, The SST transition model has been affirmed as an accurate and time-saving Reynolds-averaged Navier-Stokes (RANS) model to capture laminar-to-turbulence transitional airflow regime in lung airways (Feng et al., 2015). The model has been extensively validated with benchmark experimental data (Banko et al., 2015) in the same subject-specific respiratory system used in this study, which was documented in (Feng et al., 2017). Good agreements between our numerical simulation and independent experiments were observed, indicating the reliability of the same CFD model we employed in this study.

2.4.6. PBPK model optimization and validation

As shown in Figs. 3 and 4, PBPK model optimization and validation have been performed by comparing the in-house developed model with two experimental studies independently (Meyer et al., 1981; Savic et al., 2007). First, the average
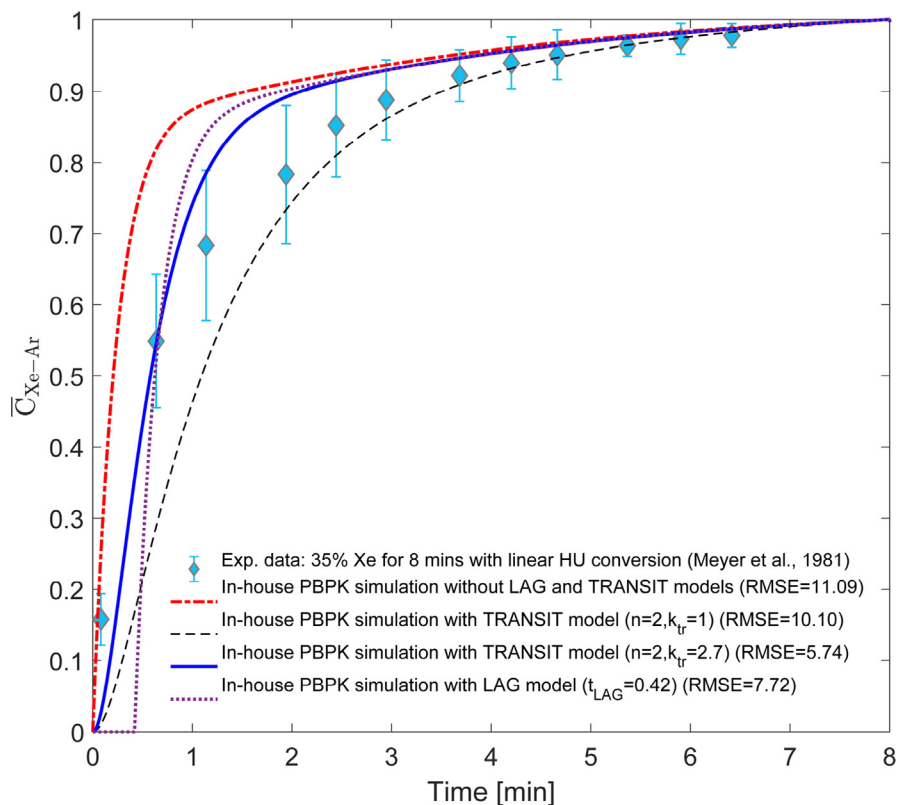
Fig. 3. PBPK model validation by comparing with an experimental study by Meyer et al. (1981).
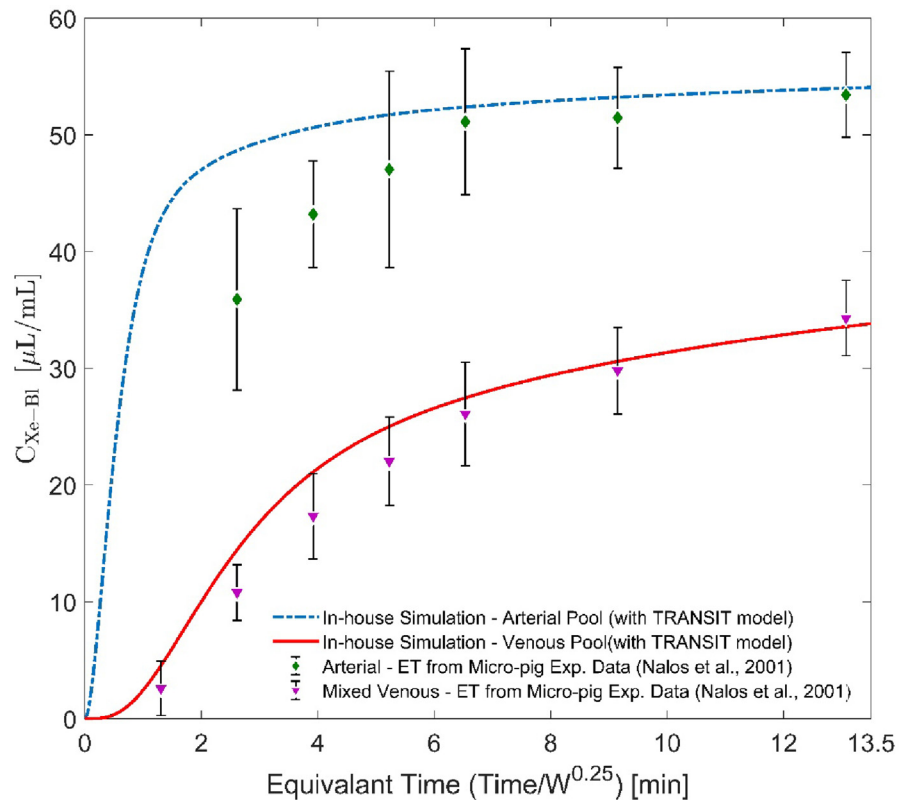
Fig. 4. The PBPK model validation with optimized TRANSIT compartments ($n = 2$ and $k_{tr} = 2.7$).

Hounsfield Unit (HU) of arterial blood converted from the end-tidal evaluation of 9 patients gathered by Meyer et al. (1981) was employed. In their experiments, xenon was inhaled for 8 minutes with a constant volume fraction equal to 35%. Fig. 3 shows the comparisons of xenon-arterial blood concentration, $\overline{C}_{Xe-Ar}$, using different delayed absorption models. The delayed absorption parameters, i.e., LAG time and TRASNIT compartments transfer coefficient, were optimized with an objective of minimizing the root mean square error (RMSE) between the numerical model and experiment data by Meyer et al. (1981). Fig. 3 indicates that the TRANSIT model can provide the best prediction by considering 2 compartments (n) with $k_{tr} = 2.70$ L/min and compared to the optimized LAG model with $t_{LAG} = 0.42$ s. In order to validate the proposed PBPK-TRANSIT model, additional independent comparisons are shown in Fig. 4, using the experimental data provided by Nalos et al. (2001) on micro-pig (25 kg) trials that studied the administration of a xenon-oxygen mixture with a volume ratio of 67:33. Animal-to-human extrapolation was performed using the scale-up method considering the equivalent time W which reflects the interspecies body weight differences. Specifically, the equivalent time W is the human-to-animal body weight ratio. Reasonable agreements can be observed in Fig. 4, indicating the reliability of the in-house PBPK-TRANSIT model. It should be noted that the PBPK model parameters reported by Katz et al. (2015) did not predict the concentration at the venous pool by providing

lower concentration predictions. Therefore, the partition coefficients are modified as specified in Section 2.2.

3. Results and discussion

3.1. Flow patterns in the human respiratory system

The simulations were performed based on different breathing patterns, i.e., a realistic breathing pattern (Case 1), and two steady-state flow inhalation patterns (Cases 2 & 3) indicating the profile of mechanical ventilation. Figs. 5 and 6 show the comparison of the airflow velocity fields at selected cross-sections in upper airways at different times for Cases 1 and 2, respectively. Velocity contours illustrate the streamwise velocity magnitude, while the in-plane vectors represent secondary flow patterns. In addition, velocity vectors are visualized at the end of the extended wall connected to the oral cavity. For Case 1, the velocity is normalized by the maximum velocity magnitude at the center of a parabolic inlet profile during the inhalation period with a value of 3.4032 m/s.

For Case 1, due to the transient respiratory flow effect, the instantaneous inlet flow rate can reach as high as 64 L/min. During inhalation, the flow transitions from laminar to turbulent in the oral cavity and pharynx as the inhalation flow rate starts from 0 and reaches its peak value at t = 0.56 s. At t = 0.56 s (see Fig. 5 (b)), the mainstream is tilted to the right hand side of the cross-section B. Due to the induced local low pressure at B, 2 counter-clockwise vortices are formed at the frontal region
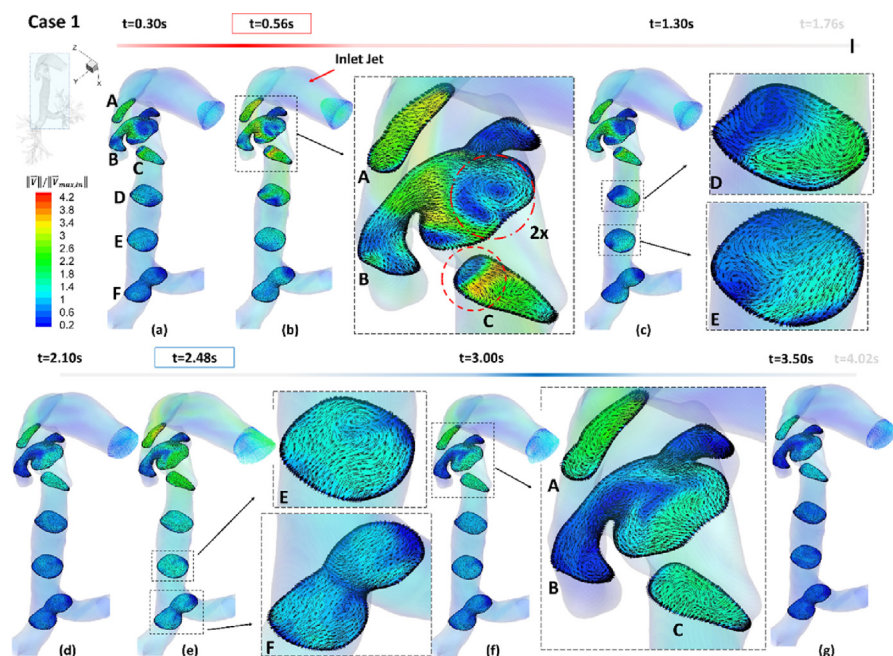

Fig. 5. Local airflow velocity distributions in the human respiratory system at different time stations for Case 1 with the realistic breathing waveform: (a) t = 0.30s, (b) t = 0.56s, (c) t = 1.30s, (d) t = 2.10s, (e) t = 2.48s, (f) t = 3.00s, (g) t = 3.50s.
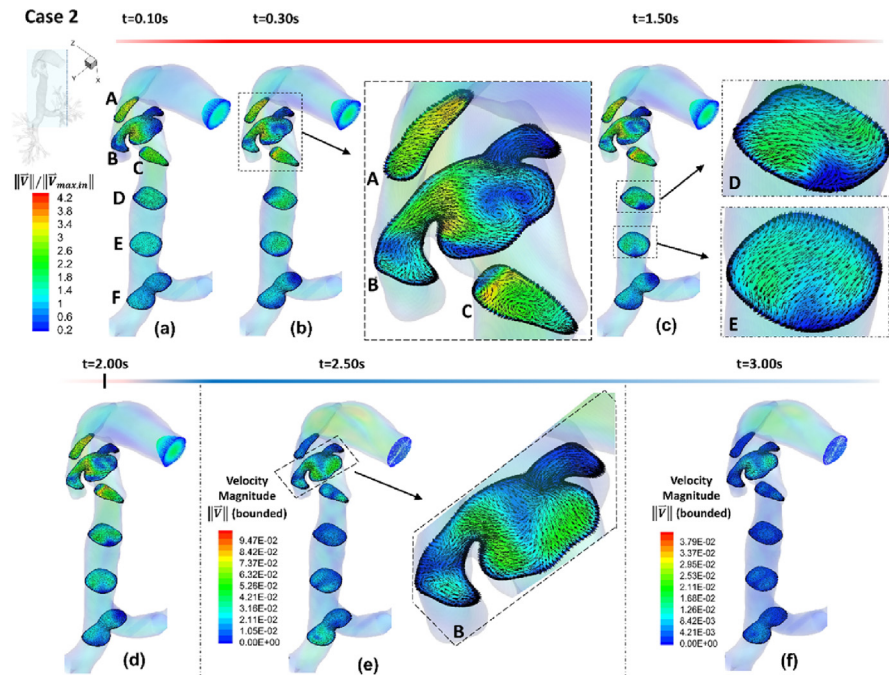
Fig. 6. Local airflow velocity distributions in the human respiratory system at different time stations for Case 2 with constant inhalation flow rate and holding time: (a) t = 0.10s, (b) t = 0.30s, (c) t = 1.50s, (d) t = 2.00s, (e) t = 2.50s, (f) t = 3.00s.

and one vortex is formed at the left-hand side (marked by the red dash-dot circle). Also, due to the effect of the laryngeal jet, a recirculation zone is generated at the back of the glottis at cross-section C. As the flow enters the trachea, circulations occur on the back side and the right side at cross-section D. Due to the mixing effect caused by the turbulent fluctuations in the trachea, airflow velocity distributes more evenly at lower sections of the trachea (see cross-section D and E at t = 0.56 s). After the first bifurcation, the flow separates and recirculation is only observed in the left bronchial tree. The reason could be that the deflection angle of the right primary bronchial is larger than that of the left primary bronchus.

During the exhalation, circulation is generated at the right primary bronchus, as shown in Fig. 5 (e) at cross-section F. As the flow moves up into the trachea, recirculation appears on the left side in cross-section E. The secondary flow occurs in oropharynx (see Fig. 5 (g)) at two sites which are visualized at cross-section B. As flow accelerates when passing the epiglottis region (see cross-section A), two vortices can also be observed which are generated due to the pressure differences at the oropharynx. Specifically, the secondary flow fields shown in Fig. 5 infer a low-pressure region at the front of oropharynx induced by the jet core, while the dead-volumes at the back of oropharynx possibly have high local pressure region.

Fig. 6 represents the velocity field for Case 2. At the mouth inlet, Re is estimated as 2,768 and it ranges from 1,953 to 4,240 in the upper airway during inhalation.

Hence, the regional flow is in the transitional regime from laminar to turbulent during inhalation. Average velocity magnitude increases from cross-sections B to C, where the area of cross-sectional C is a local minimum (130.1 mm^2). The laryngeal jet was formed, striking the posterior wall of the larynx. Deceleration can be observed as the airflow mainstream passes cross-section C. However, it is worth mentioning that during the steady-state inhalation, Re at cross-section F is 2,942 (see Fig. 6 (c)). Thus, turbulence is still expected at the first bifurcation, which may induce extra localized diffusion of the inhaled xenon thereby influencing the local absorption rate.

For Case 2 (see Fig. 6 (c)), after the flow reaches steady state during inhalation at t = 1.5 s, recirculation zones are formed in a similar region compared to Case 1 as shown in cross-section B. The difference is that the vortices generated in the pharyngeal region did not extend into the trachea during the inhalation, as the laryngeal jet effects weaken quickly and no secondary flow is observed on the cross-sections positioned at the trachea, i.e., E and D. During the holding phase starting at t = 2.5s, the velocity magnitude in the upper airways decreased below 0.01 m/s. Another observation is that the velocity magnitude at the right bronchus region is higher than that at the left bronchus. Such a phenomenon could be a result of the asymmetrical geometry structure in the oropharynx region. Explicitly, due to the asymmetrical constriction at epiglottis, there is a noticeable shift of the flow to the right, as shown in Fig. 6 (b) cross-section B. As the flow moves all the way down to the trachea and lower airways, this asymmetrical feature is preserved and eventually causes the asymmetric distribution of flow in the left and right lobes. Similar airflow patterns were found in Case 3 compared to Case 2. During inhalation, the velocity field is similar to the one presented for Case 2 (Fig. 6 (a)−(c)). Also, as long as the velocity field has reached a steady condition after t = 1.5s, a similar pattern is observed for the holding time between t = 1.5s to t = 2.5s for Case 3 as the one for Case 2 between t = 2.0s to t = 3.0s (see Fig. 6 (e)−(f)).

3.2. Xenon transport and absorption

Fig. 7 shows the normalized xenon mass fraction distribution, $\overline{f}_{Xe}$, in upper airways at a different time for all cases. $\overline{f}_{Xe}$ is defined as the ratio between the local xenon mass fraction and the inlet xenon mass fraction. The impact of transient inhalation on xenon transport is shown in Case 1 (see the top row in Fig. 7). With time evolving until the end of inhalation, $\overline{f}_{Xe}$ increases throughout the respiratory airway. As the inhalation flow rate reaches its peak value, i.e., at t = 0.56 s, the highest amount of xenon reaches the two lower lobes compared to the other three lobes.

Exhalation starts at t = 1.76 s, and $\overline{f}_{Xe}$ decreases in the lower airway regions because of expiratory removal and continuous absorption effects. The higher surface area at the lower airway regions increases the absorption and consequently the transport of
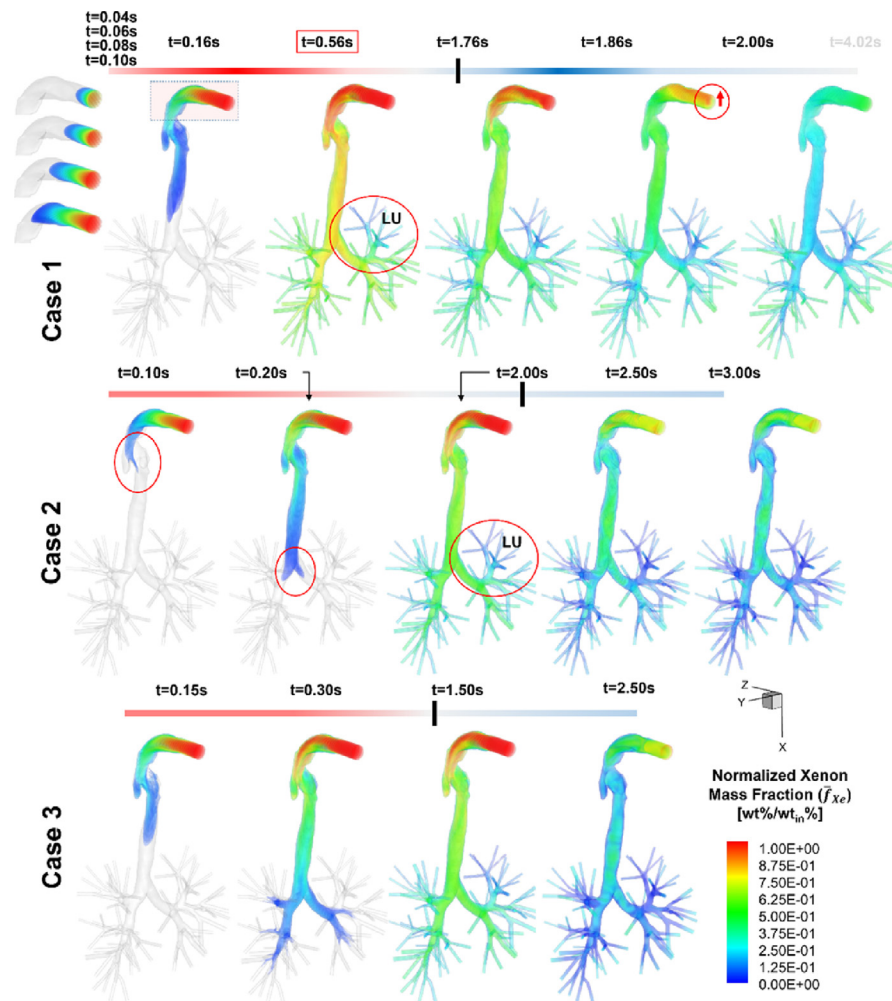
Fig. 7. Volume rendering of normalized xenon mass fraction at different times for Cases 1, 2, and 3. In Case 1, the inhalation flow rate reaches peak value (64 L/min) at t = 0.56s and exhalation starts at t = 1.76s. In Case 2 and Case 3, constant inhalations last for 2 s and 1.5 s with 1-s holding time.

the xenon from airway lumens to extrapulmonary regions. At t = 1.86 s, the exhaled xenon is propagated and touches the hard palate at the oral cavity. This observation of flow extends to the mouth inlet, which results in the exhaled jet exiting mostly from the upper section of the mouth inlet.

In the middle and bottom rows of Fig. 7, the xenon mass fraction for Cases 2 and 3 are visualized respectively. It can be observed that $\bar{f}_{Xe}$ distributions at the end of inhalation are similar, which proves that the state of equilibrium was reached between the absorption and convection of the xenon at the airway lumen. Delayed xenon mass delivery to lower airways can be observed for all three cases, indicating delayed downstream absorptions and shorter airway residence time during inhalations. However, the mentioned delayed time, i.e., 0.20 s, is short; it causes a significant difference in the uptake value after considering a repeated cycle of breathing

(Figs. 11 and 12). For both steady-state inhalation cases (Cases 2 and 3), it can be noticed that the inhalation duration has little impact on the xenon transport in human airways and $\overline{f}_{Xe}$ distributions are very similar during both inhalations and at the end of the holding time. However, differences concerning xenon transport patterns can be noticed between steady inhalations (Cases 2 and 3) and the unsteady inhalation case (Case 1). Specifically, when the flow reaches a steady state in Case 2, a small amount of xenon is transported into the lower airways, i.e., generation 5 and 6. In Case 1, however, more xenon reaches the deeper lung as the inhalation flow rate increases, which could lead to higher xenon absorption in lower airways.

Furthermore, Fig. 8 shows the distributions of xenon absorption mass flux j_{Xe} in the human respiratory system at different times. For all three cases, in upper airways to G6, xenon mass flux is mostly absorbed in the upper airway during inhalation, with high absorption rates at oropharynx and the main bronchi (see the red dash-dot circles in Fig. 8). These hotspots were formed because of the high concentration of xenon accumulated due to airflow recirculation effect.

For Case 1, at t = 0.56 s, asymmetry in j_{Xe} distributions exist in-between the left and right lobes, which is related to non-uniformly distributed flow velocity at the first bifurcation (see cross-section F in Fig. 5 (b)). At the beginning of exhalation, j_{Xe}
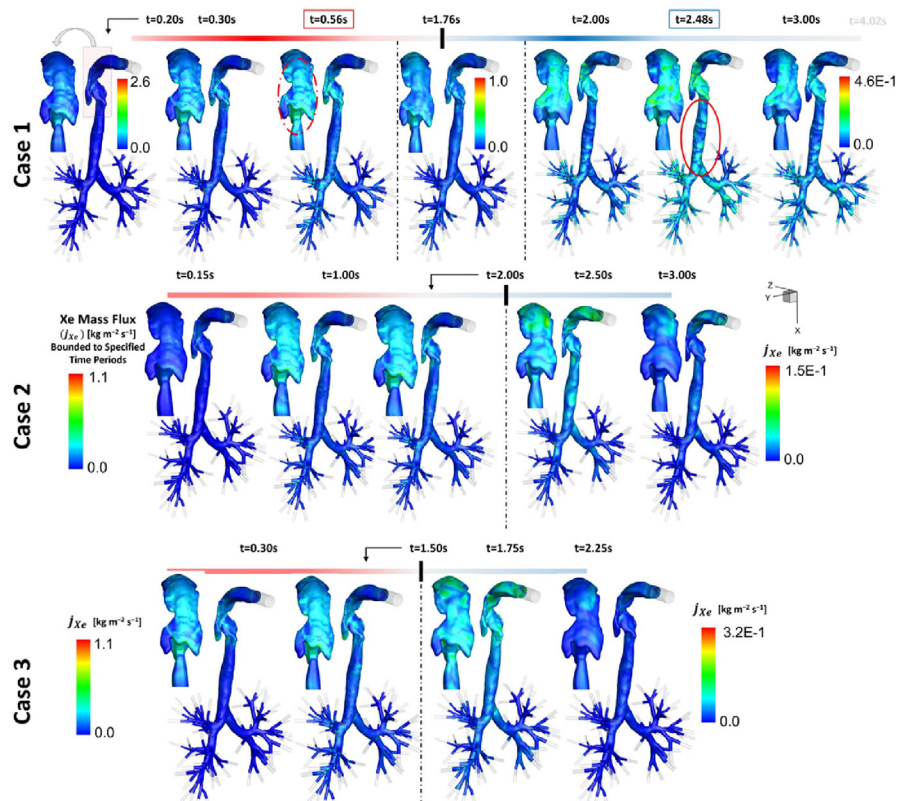

Fig. 8. Localized xenon mass flux through airway walls at different times in a single breathing cycle.

in the trachea and lower airways start to increase because $\bar{f}_{Xe}$ at G6 outlets are respired through the upper airway during exhalation. It is noticed that the left and right upper lobes have the lowest j_{Xe} compared with other lobes during exhalation.

For Cases 2 and 3, after the flow reaches steady state, high j_{Xe} can be observed at the superior part of the trachea and bifurcations in the lower airways, due to the longer residence time induced by the recirculations (see Fig. 6). As flow separates at the bifurcations, recirculation occurs, and xenon tends to accumulate near these bifurcating points. During the holding phase, xenon transport is dominated by diffusion. The evident secondary flow is observed in both the trachea and the first bifurcation, hence j_{Xe} in those two regions shows a uniform distribution.

Also, analysis of xenon transport at different lobes was executed and shown in Fig. 9. The area-weighted average (AWA) of the xenon (see Eq. (10)) absorbed by the walls was calculated for each region as shown in Fig. 9. Profiles of normalized AWA xenon mass fraction (wt %/wt$_{inspired}$ %), i.e., AWA $\bar{f}_{Xe}$, at different airway regions for Case 1 after a full breathing cycle are depicted. In general, upper respiratory tracts, including oropharynx, trachea, primary bronchi, and the carina of trachea have higher AWA $\bar{f}_{Xe}$ during a full breathing cycle. Also, AWA $\bar{f}_{Xe}$ is higher in upper airways during inhalation compared with exhalation. However, this difference is
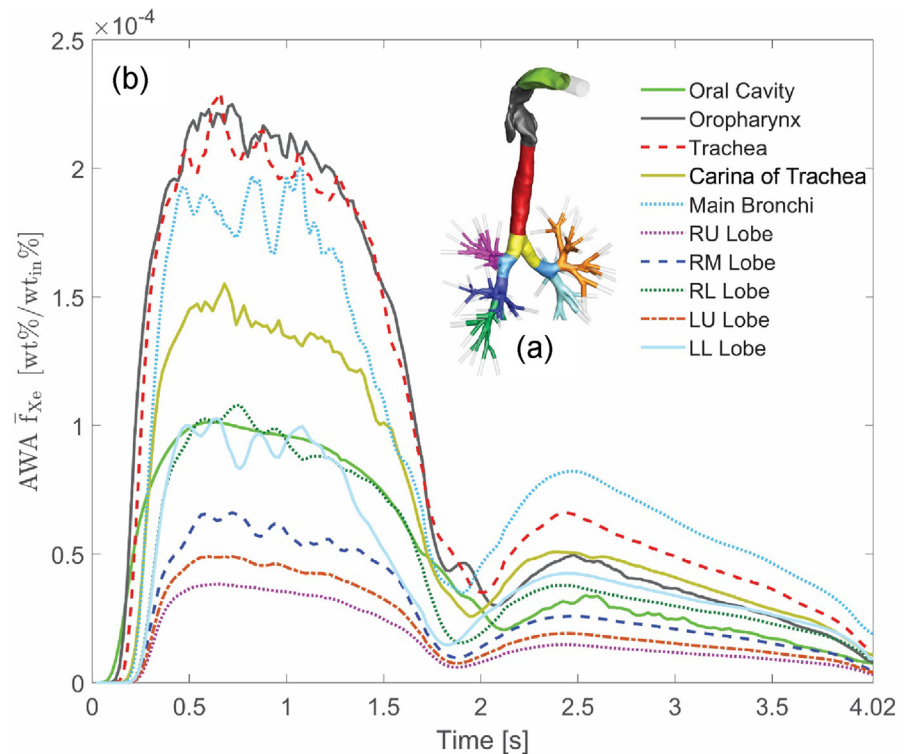

Fig. 9. Variation of xenon uptake (normalized areas weighted average mass fraction) at different lobes for Case 1 in a full inhalation-exhalation cycle): (a) the schematic of regional division; (b) regional xenon uptakes vs. time.

not obvious in the lower airway, especially for upper lobes, because of the low $\overline{f}_{Xe}$ in these regions (see Fig. 7 Case 1). Although xenon first starts to be absorbed in the oral cavity, AWA $\overline{f}_{Xe}$ profile is relatively low in this region compared with lower respiratory airway regions. The high flow velocity in the oral cavity causes short residence time of xenon in these regions, which leads to low AWA $\overline{f}_{Xe}$ field regardless of the high xenon concentrations. The oropharynx and trachea are the two regions with the highest absorption rate of xenon among all other regions during inhalation. Recirculation regions and near-wall high mass fractions of xenon are the two key factors that contribute to the high absorption rates in the oropharynx. The trachea has the highest xenon absorption during inhalation due to the decrease of flow mainstream velocity after the glottis and the recirculation induced by laryngeal jet at the back of glottis. Lower lobes have higher AWA $\overline{f}_{Xe}$ profile compared with other lobes for a full breathing cycle, which is consistent with the observation made from Fig. 7. As the airflow becomes asymmetric after the epiglottis region, the flow shifts to the right side of the airways leading to the higher mass flow rates, which caused the higher xenon uptake in this region (see Fig. 8 at t = 0.56s). Since the density of xenon is much higher than that of air, the inertial effects of xenon are stronger than air during the transport in human respiratory systems.

AWA $\overline{f}_{Xe}$ of xenon reaches the peak value at the maximum breathing flow rate, i.e., t = 0.56s. Then, xenon uptake rate decreases with fluctuation gradually until the end of inhalation, i.e., t = 1.76s. As it can be observed, there is a delayed absorption between the regions. The delayed absorption period between the oral cavity and the primary bronchi is estimated as 0.1s. At the exhalation period, delayed absorption can also be observed. During exhalation, the main bronchi have the highest xenon absorption rate. The reason is that recirculation zones are formed as the flow is mixed at the main bronchi during exhalation. Although fluctuations are noticed in the oropharynx and oral cavity, AWA $\overline{f}_{Xe}$ is lower compared to the trachea and main bronchi. The reason can be recalled by considering the increased absorption at the lower airways during the exhalation.

3.3. Translocation of xenon in systemic regions

Compared to PBPK models (Katz et al., 2015; Lockwood, 2010), one of the advantages of using the coupled CFD-PBPK model is the capability of simulating xenon translocations with realistic lung absorption data. To investigate breath pattern influence on xenon translocations, Cases 1 to 3 were investigated, and simulations were performed to predict translocation behaviors of xenon in 60 minutes. Direct estimations of arterial concentrations were provided based on different intakes.

Fig. 10 represents the moles of xenon gas (n_{Xe}), derived from the transient uptake concentrations at specified regions, i.e., upper airway to G6 and distal sections of the lung from G6 to G23. Comparisons are visualized to track n_{Xe} for all three cases
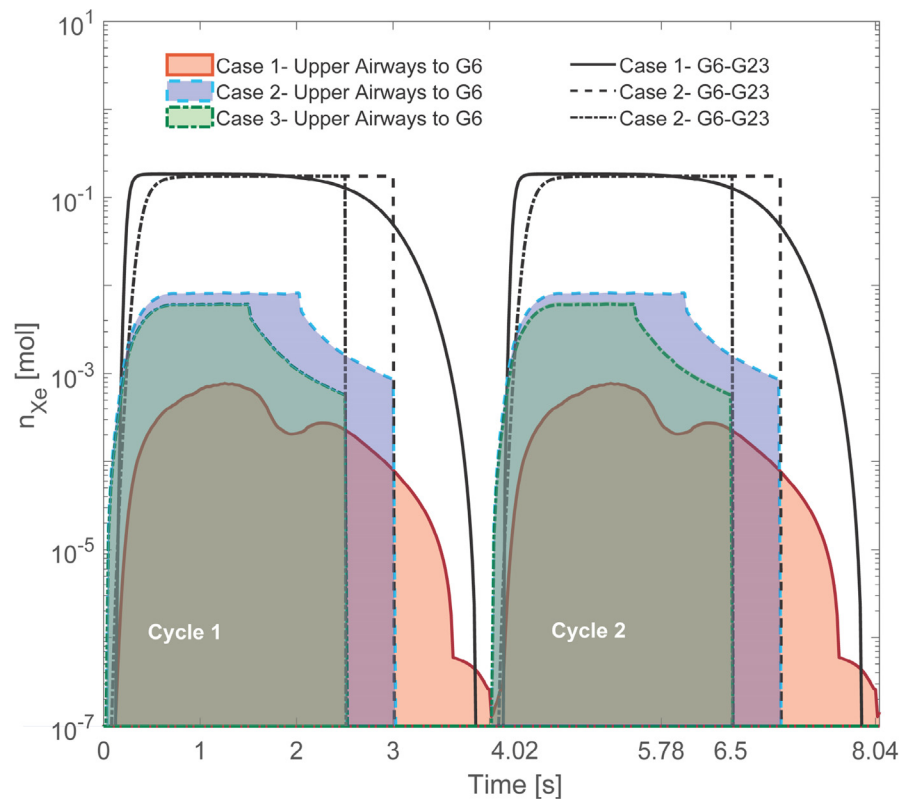
Fig. 10. Xenon uptake vs. time in different regions with different breathing patterns.

over 2 full breath cycles, in which 67% xenon and 33% oxygen were inhaled. As long as the absorption of n_{Xe} at the upper airways was not complete, a significant amount of the inspired gas is transferred to the distal sections of the lung (see Fig. 7). According to the fact mentioned above, the PBPK simulation process is separated into two parts: (1) the absorption of the xenon by tissue layers related to the upper airways (from mouth to G6), and (2) the transient transport of xenon from G6 to distal airways, and consequently the alveolar sacs. This allows for a complete profile of xenon uptake throughout different regions of the respiratory airway.

Case 1 has a very distinct breathing pattern over time for n_{Xe} compared to that of Cases 2 and 3 from mouth to G6. After an initial rapid increase of n_{Xe} during inhalation, Cases 2 and 3 show an exponential decrease of n_{Xe} during the holding time before abruptly returning to a value of zero. Case 1, on the other hand, has a much more continuous n_{Xe} profile, with a gradual rise and decline in magnitudes of n_{Xe} during inhalation and exhalation. As Fig. 10 also shows, the profile for all three cases is similar in the G6-G23 region, with exception to a difference in the exhalation period. In general, for the G6-G23 region, the magnitude of n_{Xe} rapidly increases during the inhalation period until reaching a steady value. For Cases 2 and 3, the value of n_{Xe} decreases to zero at the end of the holding period as long as a complete xenon absorption during the inhalation and holding time was assumed. However for
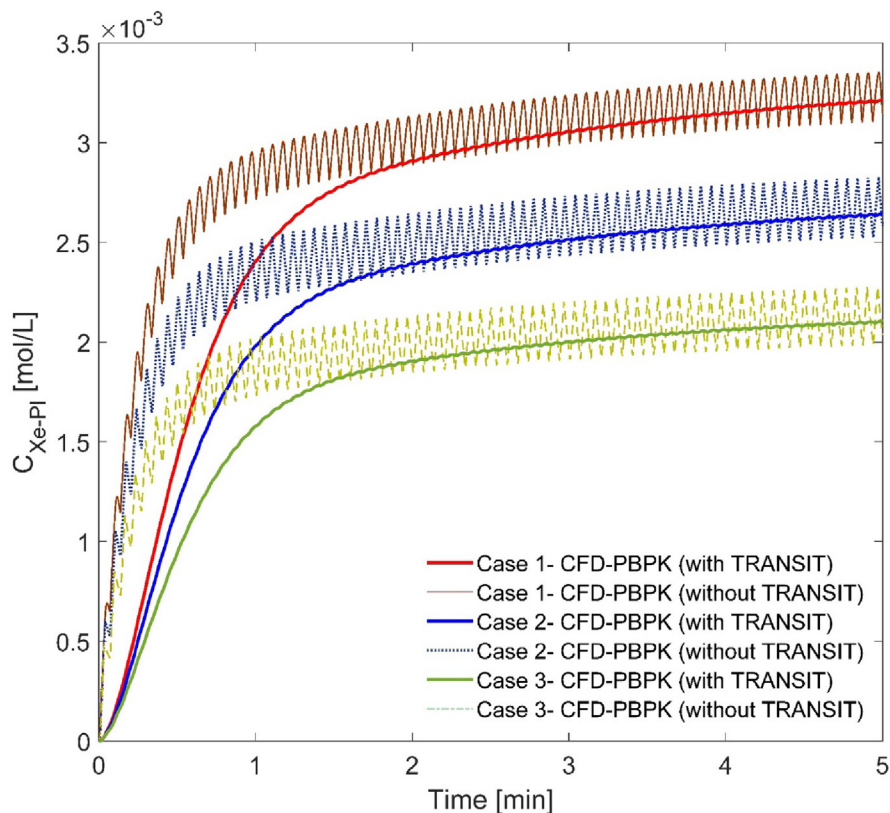
Fig. 11. Comparison of xenon-artery concentrations from 0 to 5 minutes over a 60-min period after inhaling 67% xenon and 33% oxygen with different breathing patterns.

Case 1 the value of n_{Xe} exponentially decreases during the entire exhalation period to a value of zero, i.e., the developed in-house CFD model assumption to exponentially decrease the xenon mass fraction during the exhalation at the outlets.

In the upper airways (mouth to G6), it is shown that Case 1, which has an average total tidal volume of 686 mL, sees a maximum n_{Xe} of 7.68e-4 mol. The maximum n_{Xe} is reached at the peak of inhalation flow rate, i.e., t = 0.56 s. Afterward, n_{Xe} decreases during the inhalation period. At the peak of the exhalation period, i.e., t = 1.76 s, n_{Xe} increases again to approximately 2.7e-4 mol. The increase is a result of higher xenon absorption as the exhaled xenon touches airway walls (see Fig. 9). After the first breathing cycle, n_{Xe} decreases to 1.28e-7 mol at t = 4.02s. The 2nd breathing cycle then begins at t = 4.02s with an initial value of n_{Xe} = 1.28e-7 mol. The 2nd cycle then proceeds with a pattern similar to that of the first, with slightly different magnitudes of n_{Xe} as the 2nd cycle's inhalation period starts. This is due to the absorption of the remained xenon in the respiratory system resulted from the previous cycle.

In contrast, it was observed that n_{Xe} in Case 2 has a maximum value of 8.2e-3 mol upon the completion of the 2.0-s inhalation in the upper airways (mouth to G6). At
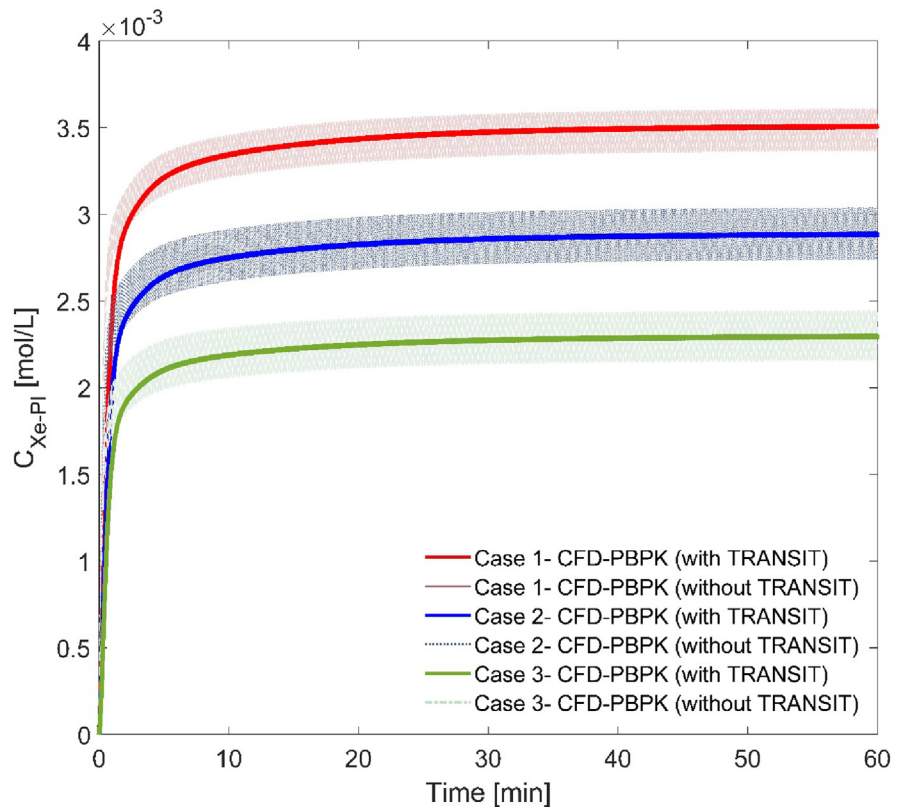
Fig. 12. Comparison of xenon-artery concentrations over a 60-min period after inhaling 67% xenon and 33% oxygen with different breathing patterns.

this point, n_{Xe} in the airway decreases exponentially to 8.6e-4 mol during the 1.0-s holding time. As for Case 3, the xenon in the airway increases to 6.2e-3 mol during the 1.5-s inhalation, before exponentially decreasing to 5.7e-4 mol during the 1.0-s holding time. The exponential decrease in n_{Xe} for both cases is a result of the decreased absorption of xenon with the holding time instead of a realistic exhalation pattern. The 2nd breathing cycle proceeds as the first one for both Cases 2 and 3, with the starting concentration of xenon being equal to zero. Compared to Case 3, the uptake of xenon is greater at each breath for Case 2 due to the higher tidal volume and the longer inhalation duration.

Furthermore, Fig. 10 shows that the maximum n_{Xe} for distal airways (G6 to G23) in Case 1 is 1.8e-1 mol. Similar to Cases 2 and 3, Case 1 shows a rapid increase of xenon uptakes until it reaches its maximum at approximately t = 0.30s. Compared to Cases 2 and 3, the delayed n_{Xe} peak is due to the realistic low flow rate at the start of inhalation in Case 1. Rather than the idealized square waveforms employed in Cases 2 and 3, realistic inhalation waveform leads to the longer residence time of xenon to reach an equilibrium in transport and absorption to the distal airways. A mild decrease of n_{Xe} occurs at t = 1.76 s before the drastic drop starting at t =

2.5 s. Cases 2 and 3 also have rapid increases in G6-G23 region, reaching the maximum uptake 0.1742 mol at t = 0.5s. The 2nd breath cycle then begins with no xenon remaining in the G6-G23 region, and the profile proceeds the same as it did during the first breathing cycle. Comparisons among the three cases demonstrate that employing idealized steady-state inhalation waveforms (Cases 2 and 3) will lead to significant differences in xenon uptake predictions, rather than using the realistic breathing waveform (Case 1). Additionally, Case 1 also reflects the reality that not all of the xenon would be exhaled with each breath. Such a phenomenon was missing in both Cases 2 and 3.

Overall, Fig. 10 shows very similar trends for the selected steady-state breath cycles, i.e., Cases 2 and 3. Although n_{Xe} magnitudes are different in the upper airways to G6 due to the change in tidal volume for these two cases, the comparison can still demonstrate that Case 1 had a significant n_{Xe} profile in the upper airways compared to that of the cases with hold time. This large discrepancy demonstrates that it is necessary to simulate the exhalation to provide more accurate predictions of uptake profile of xenon, especially in the upper airways to G6.

3.4. Xenon safety and anesthetic effectiveness

Predictions of xenon arterial concentration variations associated with multiple breathing cycles were achieved and presented in Figs. 11 and 12. Fig. 11 shows the xenon-arterial concentration C_{Xe-Pl} from 0 to 5 minutes over a total time duration of 60 minutes. Simulation results of all three cases were documented using the CFD-PBPK model both with and without the TRANSIT model. For simulation results with the TRANSIT model, the epithelial and sub-epithelial compartments that are included in the model dampen the effect of the tidal discharge into the systemic regions away from the lungs. In contrast, C_{Xe-Pl} profile oscillates with a greater amplitude when the TRANSIT model is not included. Indeed, two additional compartments are introduced as an effective dissipation to reduce the high-frequency fluctuation.

Fig. 12 shows the time course of C_{Xe-Pl} from 0 to 60 minutes. All three cases have similar trends for the C_{Xe-Pl} profile over the 60-minute duration, although the different inhalation tidal volumes for the three cases creates a different range in C_{Xe-Pl} over the time period. With a rate of 15 breaths per minute, it was determined what percentage of the maximum C_{Xe-Pl} was reached after continuous tidal volume inhalation of 67% xenon. For Case 1, the maximum C_{Xe-Pl} was 0.003509 mol/L, and 68.5% of the maximum arterial concentration was reached after 1 minute. For Case 2, the maximum C_{Xe-Pl} after one hour was determined to be 0.002888 mol/L, and 68.65% of the maximum arterial concentration was reached in 1 minute. For Case 3, the arterial concentration was the lowest, with a maximum value of 0.002298 mol/L, and 68.75% of the maximum concentration being reached after 1

minute. The comparison demonstrates that for the three cases with different tidal volumes, the rate of C_{Xe-Pl} increase is not significantly influenced by breathing patterns.

A previous study determined that the average induction time when a loss of consciousness is experienced in patients with use of xenon anesthesia is about 71 s (Nakata et al., 1997). For the three cases in this study, it was determined what fraction of the maximum C_{Xe-Pl} was reached after 71 s. This was then calculated to determine a benchmark concentration that is needed in each case to induce patient unconsciousness. Cases 1 and 3 reported the largest difference in the fraction of maximum concentration reached after 71s of inhalation for the TRANSIT scenarios. In case 1, C_{Xe-Pl} reached 0.002996 mol/L after 71 s, which is 85.4% of the xenon concentration after 60 minutes of administration. In Case 3, however, C_{Xe-Pl} reached 0.001694 mol/L, which is only 79.4% of its maximum value. As for the cases without TRANSIT, the fraction of the maximum concentration reached was similar for all three cases. The largest difference for the cases without TRANSIT was between Case 1 and 2. Case 1 reported that after 71s of inhalation, C_{Xe-Pl} reached 0.002580 mol/L, which is 75.6% of its maximum value after 60 minutes. C_{Xe-Pl} reached 0.002125 mol/L after 71s, which is 73.7% of its maximum C_{Xe-Pl}. The difference in C_{Xe-Pl} for all three cases, both with and without TRANSIT, provide insight into the impact of a different tidal volume on the concentration reached after the 71s time period, i.e., the estimated xenon induction period.

Another previous clinical study determined the emergence time from xenon anesthesia in 30 patients, with 4 different methods being used to qualify what equates to emergence (Goto et al., 1997). These 4 methods noted emergence after wash-out times of approximately 3.4 (the time until the patient opened her eyes), 3.6 (was judged ready for extubation), 5.2 (could correctly state her name and date of birth), and 6.0 (could count backward from 10 to 1) minutes. By looking at C_{Xe-Pl} for Case 1 in Fig. 13, the results can give an idea on what the remaining C_{Xe-Pl} is after the time points that were determined to induce emergence from anesthesia in the patients. First, it should be noted that after the final inhalation of xenon at t = 60 min, the maximum C_{Xe-Pl} is approximately 0.00362 mol/L. Also, the first breathing cycle after the administration period contributes to a small amount of xenon transport to the system regions. This is because of the existing unabsorbed gas in the lungs during the previous breathing cycle. A period of 0.56s, i.e., time of the peak inhalation flow rate, is assumed with the xenon concentration as the maximum C_{Xe-Pl} during the administration. Following the completion of inhalation, the wash-out of xenon begins over a period of the next several minutes. For the realistic breathing pattern with exhalation, after 3.4 minutes of xenon wash-out, only 9.7% of the maximum C_{Xe-Pl} was still remaining in the arterial pool. After 3.6 minutes of wash-out, 9.3% of the maximum C_{Xe-Pl} is remaining, while there is 7.2% of the maximum of the maximum C_{Xe-Pl} remaining 5.2 minutes after starting xenon
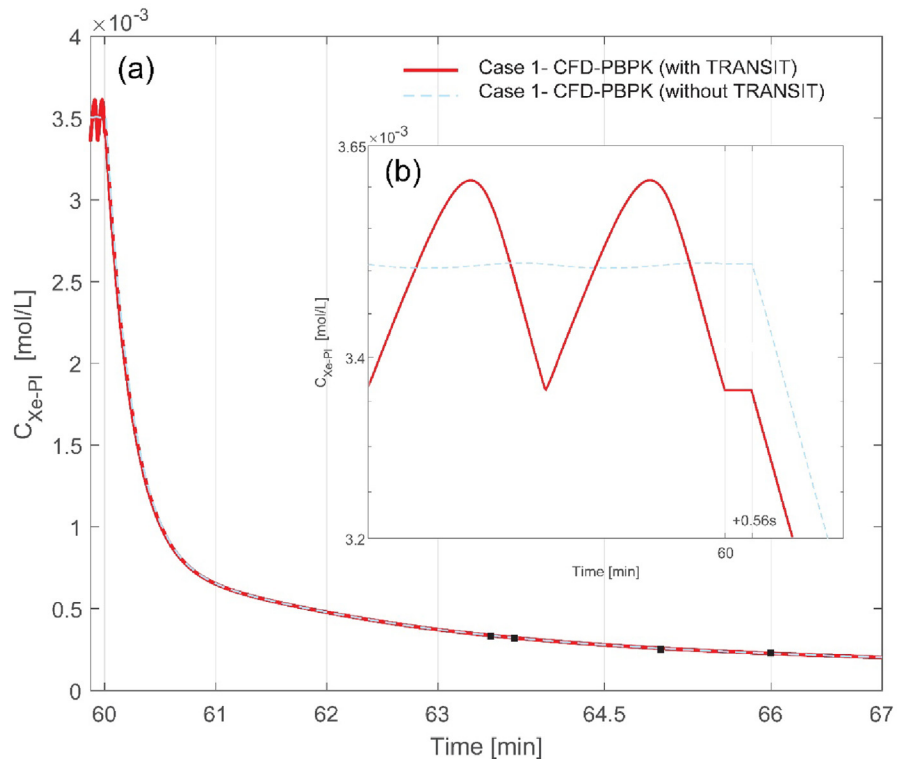
Fig. 13. Comparison of xenon-arterial concentrations between models with and without TRANSIT compartments during the emergence after respiration of 67% xenon: (a) concentration vs. time from 0 to 67 min; (b) The enlarged graph of concentration vs. time from 0 to 60 min.

wash-out. Finally, at the greatest time measured for patient emergence, only 6.5% of the maximum C_{Xe-Pl} is remaining. These numbers are used to determine a benchmark C_{Xe-Pl} to indicate when the emergence from anesthesia is expected to occur. For all four time points, C_{Xe-Pl} is reduced by more than 90%.

By using a different inhalation tidal volume in each case, a change in the xenon-arterial concentration is observed in different cases. Case 1, which has an average inhalation tidal volume of 772 mL (the mean exhalation tidal volume of 601 mL, and the average total tidal volume of 686 mL), resulted in an arterial concentration with a maximum value of 0.003509 mol/L (see Fig. 12). This concentration is 16% higher than the maximum concentration for Case 2, which is equal to 0.002887 mol/L and has a tidal volume of 750 mL. With a tidal volume of 500 mL, Case 3 resulted in a maximum arterial concentration of 0.002298 mol/L, which is 34.5% lower than the concentration measured for Case 1. Also, xenon translocations into the systemic regions were compared after the first breath in Cases 2 and 3. The comparison shows that with a 50% increase in the tidal volume (from 500 to 750 mL), C_{Xe-Pl} increases by 24% (0.0004827−0.0005991 mol/L) after a single first breath. However, this comparison between Cases 1 and 2 with inhalation tidal volumes of 750 and 772 mL respectively (3% increase), shows 15% (0.0006914−0.0005991 mol/L) increase

of C_{Xe-Pl} after the first breath. The higher inhalation tidal volume with a longer duration through the morphology of the respiratory airways resulted in a considerably higher concentration of xenon at the distal sections of the lung, pulmonary arteries, and consequently systemic regions. Observations made based on Fig. 7 are similar for the xenon mass fraction at the peak volumetric flow rate of Case 1. Thus, the case with the realistic breathing pattern resulted in the highest arterial concentration, and subsequently the highest effectiveness of xenon.

Overall, Figs. 11, 12, and 13 demonstrate the difference between the model with and without the implementation of TRANSIT. As the more accurate model (see Sections 2.4.5 & 2.4.6), the CFD-PBPK model with TRANSIT limits the oscillatory behavior in the C_{Xe-Pl} profile, and a much more steady increase of C_{Xe-Pl} is observed. These results show that in patients with different tidal volumes, inhalation of a xenon anesthetic can result in drastically different concentrations of the substance in the body. As mentioned in the literature review, the MAC that was selected in other studies for maximum effectiveness with safety considerations ranged from 50-70%. This study utilized a MAC that was 67% of the tidal volume for all three cases, and the results showed a considerable range of change for xenon arterial concentrations between cases. Since there is such a large difference in concentrations between cases, it would be advisable to perform trials in a clinical setting to determine the safety range of xenon arterial concentrations that would still be effective for medical procedures.

4. Conclusions

A CFD-PBPK model was developed to investigate the xenon transport, absorption, and translocation from a patient-specific human respiratory system to systemic regions with a realistic respiratory waveform and two steady-state inhalation conditions. Incorporating the CFD model can precisely predict the transient lung uptake of xenon on a breath-by-breath basis and provide more realistic inputs to the PBPK model, rather than a simple measurement of continuous uptake like that of the standalone PBPK model. Numerical results demonstrated the capability of the multiscale model to capture the concentration increase of xenon in the respiratory system over time during multiple consecutive inspiration-expiration cycles. Concerning the effectiveness and potential health risks of administrating xenon gas with different breathing patterns, quantitative conclusions can be summarized as follows:

(1) Incorporating TRANSIT compartments to the CFD-PBPK model is necessary, which enhances the prediction accuracy of xenon translocation compared to experimental data;

(2) Xenon absorption rates are not evenly distributed in five lobes. Lower lobes have higher absorption rates compared to the other three lobes;

(3) Breathing patterns have a significant influence on the accuracy of xenon absorption and translocation. Therefore, precise breathing waveforms must be employed in the CFD-PBPK modeling process;

(4) For the cases with steady inhalation flow rates (Case 2 & 3), i.e., presenting the mechanical ventilation, by implementing a 50% increase in the tidal volume (from 500 to 750 mL), the xenon-arterial concentration has increased by 24% (0.0004827−0.0005991 mol/L) after the first breath and has increased by 26% (0.002887−0.002298 mol/L) after 60 minutes of xenon administration; and

(5) For the case using the realistic inhalation-exhalation waveform (Case 1), with an inhalation tidal volume of 772 mL (3% more than Case 2), results show a xenon-arterial concentration of 0.0006914 mol/L, ie., 15% more than Case 2, after the first breath and 0.002887 mol/L, i.e., 16% more than Case 2 after 60 minutes of xenon administration.

The experimentally validated CFD-PBPK model provides great potential for future use as a reliable noninvasive tool for multiple patient-specific pulmonary healthcare studies. Specifically, the multiscale model is improved from the first version (Haghnegahdar et al., 2018) by:

(1) Incorporating a full breathing cycle and absorption delay model; and

(2) Integrating transient mass flux couplings at the interface between lung airways and systemic regions for both upper airways and distal airways.

Future refinements of the CFD-PBPK model and anesthetic effect studies include:

(1) Integrating thermodynamics and bio-reactions at the sites of airway tissues;

(2) Investigating inter-subject variability between healthy people and patients with restrictive and obstructive lung diseases on the administration effectiveness and health risks of xenon and other pulmonary drug aerosols;

(3) Employing the in-house whole-lung model; and

(4) Incorporating nasotracheal or tracheal incubation tubes into the geometry, due to the fact that a tube is inserted to prevent a patient's glottis from closing after losing consciousness when undergoing anesthesia.

Declarations

Author contribution statement

Ahmadreza Haghnegahdar, Jianan Zhao, Max Kozak, and Patrick Williamson: Performed the experiments; Analyzed and interpreted the data; Contributed reagents, materials, analysis tools or data; Wrote the paper.

Yu Feng: Conceived and designed the experiments; Analyzed and interpreted the data; Contributed reagents, materials, analysis tools or data; Wrote the paper.

Competing interest statement

The authors declare no conflict of interest.

Additional information

No additional information is available for this paper.

References

Banko, A.J., Coletti, F., Schiavazzi, D., Elkins, C.J., Eaton, J.K., 2015. Three-dimensional inspiratory flow in the upper and central human airways. Exp. Fluid 56 (6), 117.

Barrett, K.E., 2010. Ganong's Review of Medical Physiology. McGraw-Hill Medical, New York, NY.

Bedi, A., Murray, J.M., Dingley, J., Stevenson, M.A., Fee, J.H., 2003. Use of xenon as a sedative for patients receiving critical care. Crit. Care Med. 31 (10), 2470−2477.

Coburn, M., Maze, M., Franks, N.P., 2008. The neuroprotective effects of xenon and helium in an in vitro model of traumatic brain injury. Crit. Care Med. 36 (2), 588−595.

Eger, E., 2001. Age, minimum alveolar anesthetic concentration, and minimum alveolar anesthetic concentration-awake. Anesth. Analg. 93 (4), 947−953.

Feng, Y., Kleinstreuer, C., Castro, N., Rostami, A., 2016. Computational transport, phase change and deposition analysis of inhaled multicomponent droplet−vapor mixtures in an idealized human upper lung model. J. Aerosol Sci. 96, 96−123.

Feng, Y., Kleinstreuer, C., Rostami, A., 2015. Evaporation and Condensation of Multicomponent Electronic Cigarette Droplets and Conventional Cigarette Smoke Particles in an Idealized G3−G6 Triple Bifurcating Unit, vol. 80.

Feng, Y., Zhao, J., Chen, X., Lin, J., 2017. An in silico subject-variability study of upper airway morphological influence on the airflow regime in a tracheobronchial tree. Bioengineering 4 (4), 90.

Goto, T., Nakata, Y., Morita, S., 2002. The minimum alveolar concentration of xenon in the elderly is sex-dependent. Anesthesiol. J. Am. Soc. Anesthesiol. 97 (5), 1129−1132.

Goto, T., Saito, H., Shinkai, M., Nakata, Y., Ichinose, F., Morita, S., 1997. Xenon provides faster emergence from anesthesia than does nitrous oxide-sevoflurane or nitrous oxide-isoflurane. Anesthesiol. J. Am. Soc. Anesthesiol. 86 (6), 1273−1278.

Goto, T., Suwa, K., Uezono, S., Ichinose, F., Uchiyama, M., Morita, S., 1998. The blood-gas partition coefficient of xenon may be lower than generally accepted. Br. J. Anaesth. 80 (2), 255−256.

Haghnegahdar, A., Feng, Y., Chen, X., Lin, J., 2018. Computational analysis of deposition and translocation of inhaled nicotine and acrolein in the human body with e-cigarette puffing topographies. Aerosol Sci. Technol. 52 (5), 483−493.

ICRP, 1994. Human respiratory tract model for radiological protection. ICRP publication 66. Ann. ICRP 24, 1−3.

Katz, I., Murdock, J., Palgen, M., Pype, J., Caillibotte, G., 2015. Pharmacokinetic analysis of the chronic administration of the inert gases Xe and Ar using a physiological based model. Med. Gas Res. 5, 8.

Keyhani, K., Scherer, P.W., Mozell, M.M., 1997. A numerical model of nasal odorant transport for the analysis of human olfaction. J. Theor. Biol. 186 (3), 279−301.

Lesieur, M., Moreau, R., 2008. Turbulence in Fluids, Vol. 40. Dordrecht: Springer Netherlands, Dordrecht.

Lockwood, G., 2010. Theoretical context-sensitive elimination times for inhalation anaesthetics. Br. J. Anaesth. 104 (5), 648−655.

Luttropp, H., Romner, B., Perhag, L., Eskilsson, J., Fredriksen, S., Werner, O., 1993. Left ventricular performance and cerebral haemodynamics during xenon

anaesthesia: a transoesophageal echocardiography and transcranial Doppler sonography study. Anaesthesia 48 (12), 1045−1049.

Lynch, C., Baum, J., Tenbrinck, R., Weiskopf, R.B., 2000. Xenon anesthesia. Anesthesiol. J. Am. Soc. Anesthesiol. 92 (3), 865−870.

Menter, F., Langtry, R., Völker, S., 2006a. Transition modelling for general purpose CFD codes. Flow Turbul. Combust. 77 (1), 277−303.

Menter, F.R., Langtry, R.B., Likki, S., Suzen, Y., Huang, P., Völker, S., 2006b. A correlation-based transition model using local variables—Part I: model formulation. J. Turbomach. 128 (3), 413−422.

Meyer, J.S., Hayman, L.A., Amano, T., Nakajima, S., Shaw, T., Lauzon, P., et al., 1981. Mapping local blood flow of human brain by CT scanning during stable xenon inhalation. Stroke 12 (4), 426−436.

Nakata, Y., Goto, T., Morita, S., 1997. Comparison of inhalation inductions with xenon and sevoflurane. Acta Anaesthesiol. Scand. 41 (9), 1157−1161.

Nalos, M., Wachter, U., Pittner, A., Georgieff, M., Radermacher, P., Froeba, G., 2001. Arterial and mixed venous xenon blood concentrations in pigs during wash-in of inhalational anaesthesia. Br. J. Anaesth. 87 (3), 497−498.

Reinelt, H., Marx, T., Kotzerke, J., Topalidis, P., Luederwald, S., Armbruster, S., et al., 2002. Hepatic function during xenon anesthesia in pigs. Acta Anaesthesiol. Scand. 46 (6), 713−716.

Sanders, R., Franks, N., Maze, M., 2003. Xenon: no stranger to anaesthesia. Br. J. Anaesth. 91 (5), 709−717.

Sanders, R.D., Ma, D., Maze, M., 2005. Xenon: elemental anaesthesia in clinical practice. Br. Med. Bull. 71 (1), 115−135.

Savic, R.M., Jonker, D.M., Kerbusch, T., Karlsson, M.O., 2007. Implementation of a transit compartment model for describing drug absorption in pharmacokinetic studies. J. Pharmacokinet. Pharmacodyn. 34 (5), 711−726.

Scheinherr, A., Bailly, L., Boiron, O., Lagier, A., Legou, T., Pichelin, M., et al., 2015. Realistic glottal motion and airflow rate during human breathing. Med. Eng. Phys. 37 (9), 829−839.

Stoppe, C., Rimek, A., Rossaint, R., Rex, S., Stevanovic, A., Schalte, G., et al., 2013. Xenon consumption during general surgery: a retrospective observational study. Med. Gas Res. 3 (12).

Treybal, R.E., 1980. Mass Transfer Operations. New York.

Weingärtner, H., Haselmeier, R., Holz, M., 1992. 129Xe NMR as a new tool for studying gas diffusion in liquids: self-diffusion of xenon in water. Chem. Phys. Lett. 195 (5-6), 596−601.

Wilcox, D.C., 1998. Turbulence Modeling for CFD, Vol. 2. DCW industries La Canada, CA.

Zhang, Z., Kleinstreuer, C., 2011. Laminar-to-turbulent fluid−nanoparticle dynamics simulations: model comparisons and nanoparticle-deposition applications. Int. J. Numer. Meth. Biomed. Eng. 27 (12), 1930−1950.

Zhang, Z., Kleinstreuer, C., Hyun, S., 2012a. Size-change and deposition of conventional and composite cigarette smoke particles during inhalation in a subject-specific airway model. J. Aerosol Sci. 46, 34−52.

Zhang, Z., Kleinstreuer, C., Feng, Y., 2012b. Vapor deposition during cigarette smoke inhalation in subject-specific human airway model. J. Aerosol Sci. 53, 40−60.